Dependence of fretting wear resistance on the α morphology and stress-induced martensite transformation in a metastable β titanium alloy

Xu, Xiaojun; Long, Jianjun; Zhang, Xiage; Dong, Yiting; Gan, Binbin; Li, Hao; Zhu, Minhao

DOI
10.1016/j.jallcom.2024.177259

Publication date
2025

Document Version
Final published version

Published in
Journal of Alloys and Compounds

Journal of Alloys and Compounds 1010 (2025) 177259

Contents lists available at ScienceDirect

Journal of Alloys and Compounds

journal homepage: www.elsevier.com/locate/jalcom

Dependence of fretting wear resistance on the α morphology and stress-induced martensite transformation in a metastable β titanium alloy

Xiaojun Xu [a,b,*], Jianjun Long [a], Xiage Zhang [a], Yiting Dong [a], Binbin Gan [a], Hao Li [a], Minhao Zhu [a]

[a] Key Laboratory of Advanced Technologies of Materials (Ministry of Education), School of Materials Science and Engineering, Southwest Jiaotong University, Chengdu 610031, China

[b] Novel Aerospace Materials group, Faculty of Aerospace Engineering, Delft University of Technology, Delft 2629HS, the Netherlands

ARTICLE INFO

Keywords:
Metastable β titanium alloy
α morphology
Fretting wear
Stress-induced martensite transformation
Plastic deformation

ABSTRACT

Systematic experimental investigations concerning the influence of α morphology on the fretting wear behaviors of metastable β titanium alloys are carried out. A Ti-10V-2Fe-3Al titanium alloy was subjected to different heat treatment routes to create dual phase microstructures consisted of β phase plus α phase with three different morphologies. The effect of α morphology on the fretting wear resistance, the resulting failure mechanisms, and stress induced martensite transformation (SIMT) were unraveled. Results show that the α morphology has a significant influence on fretting wear behaviors depending on the fretting run regimes. In the partial slip regime (PSR) and mixed fretting regime (MFR), the microstructure with lath α morphology has a lowest fretting wear volume accompanied by relatively strong SIMT effect. While in gloss slip regime (GSR), the globular α microstructure has a lowest fretting wear volume along with strongest SIMT response, yet a highest fretting wear volume for the acicular α morphology microstructure due to its brittleness nature. The subsurface observations demonstrates that a compacted and thick plastic deformation layer, especially for the mechanical mixture layer, can well protect the material surface against the fretting wear damage.

1. Introduction

Fretting wear is a surface damage phenomenon when two contact surfaces are subjected to oscillatory movement of small amplitude. It would cause the removal of surface materials and the development of internal fatigue cracks, consequently resulting in the premature failures and hence reducing the service life of the working components [1,2]. There have been numerous experiments conducted to study the fretting wear behavior so as to mitigate the fretting damages and hence improve the resistance to fretting wear [3–8]. Fretting damage has increasingly become a significant problem for many tight fit assemblies in aerospace [9–11], nuclear power plant [12,13], naval craft [14,15], and so on. Given the outstanding mechanical properties, especially the high specific strength, low density and good corrosion resistance, titanium alloys have been widely used as the key components of tight fit assemblies in such applications stated above, such as bolts, rivets and dovetail joint, which are always suffered from fretting wear damage [16,17]. Because of the low shear resistance and work hardening ability, however, titanium alloys have always been considered to have poor fretting wear resistance, which hence limits their applications where the fretting wear plays a key role [18–20].

For the titanium alloys, in the past decades, many works have been carried out to investigate their fretting wear behavior aiming to improve the fretting wear resistance. Song et al. [21] investigated the wear behavior of TiAlNb alloy with lamellar microstructures under different loads and displacement amplitudes, which indicated that the higher load and lower displacement amplitude would reduce the fretting wear. Pu et al. [22] also reported the effect of the alternate load ratio (i.e., the minimum/the maximum in sinusoidal loading curve) on the fretting wear behaviors of Ti6Al4V alloy, depending on the displacement amplitudes. It showed that at the small displacement amplitude, the fretting wear loss increased with decreasing the load ratio, but the opposite held at the large displacement amplitudes. Moreover, Waterhouse et al. [23] investigated the effect of high temperature on the fretting wear of four titanium alloys. It indicated that a compacted oxide film will be formed during the fretting wear process at high temperature, which eventually

* Correspondence to: Key Laboratory of Advanced Technologies of Materials (Ministry of Education), School of Materials Science and Engineering, Southwest Jiaotong University, Chengdu 610031, PR China.

E-mail addresses: xiaojunxu@swjtu.edu.cn, xiaojunxu0617@126.com (X. Xu).

https://doi.org/10.1016/j.jallcom.2024.177259
Received 1 August 2024; Received in revised form 22 October 2024; Accepted 24 October 2024
Available online 25 October 2024

resulted in a lower coefficient of friction and a reduced wear rate. However, Zhang et al. [24,25] commented that the sensitivity to fretting damage can be enhanced with the temperature increases for Ti811 alloy. In addition, the working atmosphere is one of the critical parameters as well. Cheng et al. [26] studied the fretting wear behavior of Ti6Al4V alloys subjected to different atmospheres, i.e., nitrogen, argon and air atmosphere. The results showed that the Ti6Al4V alloy under nitrogen and argon atmosphere had a higher wear volume as a result of the formed titanium nitride (i.e., Ti_2O_3 and TiO), which were considered to be detrimental for fretting wear resistance [27]. In addition, the study on the fretting damage modelling of the alloys has already received increasing attention [28–30], Shen et al. [30] has developed a continuum damage mechanics-based method involving debris layer evolution to predict the fretting wear and fatigue lifetime of Ti-6Al-4V under different displacement amplitudes. Notwithstanding a significant progress in understanding of fretting wear resistance and influential factors for the titanium alloys, the current study mainly focuses on the test conditions for a given titanium alloy.

It is known that fretting wear is a complex response of a material in a tribo-system depending not only on the test conditions [4,31], but even more so on the microstructural features [32,33]. Therefore, an alternative and attractive motivation is to link the fretting wear resistance to the microstructural features of titanium alloys. In comparison to the α-Ti and (α+β)-Ti alloys, the metastable β titanium alloys possess outstanding mechanical properties due to the strong tunability of microstructures via the heat treatment [34–37], especially the reinforcement in strength and work hardenability via stress induced martensitic transformation (SIMT) [38], which makes it has a great potential for the development of high wear resistant titanium. So far, some investigations have been carried out to focus on the mechanical properties as a function of microstructural features for metastable β titanium alloys. As reviewed in Ref. [39–42], α phase in metastable β titanium alloys has the critical influence in determining the final mechanical properties, including the wear resistance [32,43,44]. It is reported [45,46] that the α phase is related to the stability of metastable β phase and prefers triggering the dislocation slip to the SIMT effect, which would promote an increase in strength. Li et al. [47] further commented that the metastable β phase is more sensitive to the globular α phase than acicular α phase. Zhu et al. [41] pointed out that globular α phase could activate more dislocations and hence coordinate the plastic deformation with the metastable β matrix than the acicular α phase, hence improving the ductility. Moreover, many studies [48–50] have revealed that the SIMT effect plays a very important role in improving the tensile strength of metastable β titanium alloys while maintaining a high level of plasticity. The results show that SIMT effect occurred during tensile/compressive process could refine the initial β grains, which would create a dynamic Hall-Patch effect, hence leading to the effective improvement of the work hardening ability [50–52]. Wang et al. [53] reported that SIMT effect would not only delay the damage nucleation, but also prevent the crack propagation, eventually achieving superior fatigue limit. While Xiao et al. [54] pointed out that SIMT has two effects on damage response, which depend on the spacing between the formed martensitic laths, i.e., 1) the small martensitic lath spacing would blunt the cracks tips, hence to some extent inhibit the crack propagation, 2) the large martensitic lath spacing would facilitate the crack nucleation at the phase boundaries. Nonetheless, these works mainly focus on the studies on the mechanical properties of metastable β titanium alloys, yet less studies on fretting wear behavior. In particular, the effect of α phase on fretting wear resistance and the resulting stress induced martensite transformation (SIMT) response during fretting wear for the metastable β titanium alloy is still unclear yet.

Given the outstanding issues discussed above, in the present study three different heat treatment routes were designed to obtain different morphologies of α phase in metastable β matrix, aiming to clarify the effect of microstructural features with respect to the varied α morphology on the fretting wear behavior as well as SIMT mechanism.

Table 1
the chemical composition (wt%) of the as-received Ti-10V-2Fe-3Al alloy.

Chemical composition (wt%)							
Elements	V	Fe	Al	O	N	C	Ti
Ti-10V-2Fe-3Al	10.53	1.85	2.94	0.10	0.02	0.005	Bal.

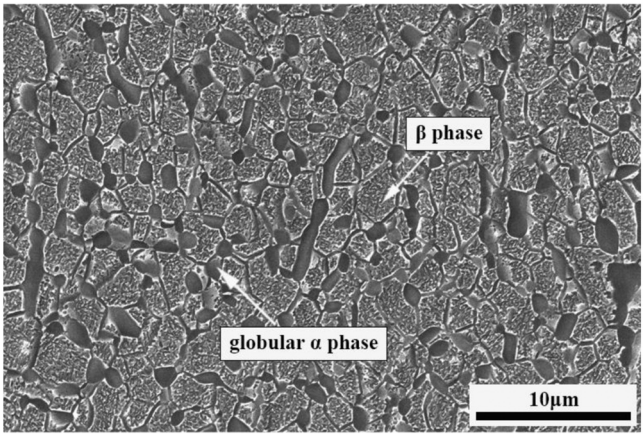

Fig. 1. The microstructure of the as-received Ti-10V-2Fe-3Al alloy.

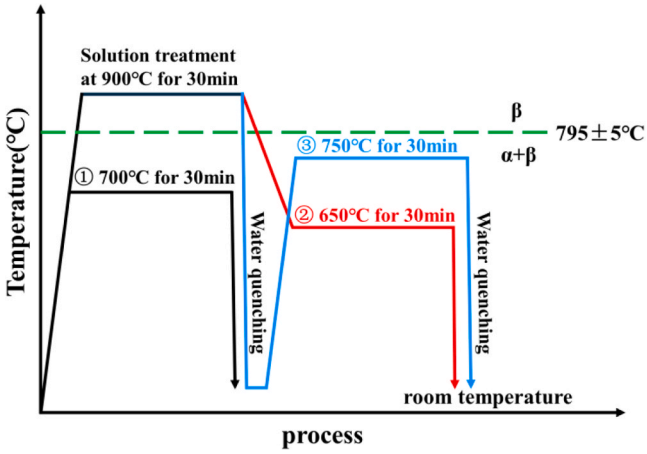

Fig. 2. Schematic illustration of different heat treatment process routes: ① the α+β phase field heat treatment, ② the β+(α+β) phase field heat treatment, and ③ the β+quenching+(α+β) phase field heat treatment.

In order to separate the effects of α phase volume fraction from that of the morphology, the volume fractions of the α phase were intentionally tailored by heat treatment to keep a same level. The fretting wear behavior of the metastable β titanium alloy samples with different morphologies are studied by using fretting wear test rig designed under different fretting running regimes. The worn scar and the evolution of the subsurface microstructures were observed to reveal the different response of various morphological features on the SIMT effect, fretting wear resistance and failure mechanism.

2. Experimental procedures

2.1. Materials and heat treatments

A raw material chosen in the current study is a typical metastable β titanium alloy (Ti-10V-2Fe-3Al), which was provided by Institute of Metal Research, Chinese Academy of Sciences. The resulting chemical composition (in wt%) of the as-received material was listed in Table 1.

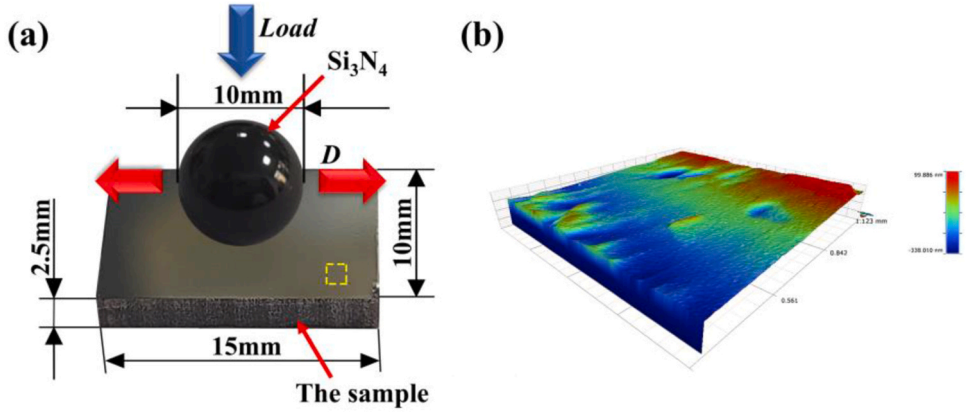

Fig. 3. A schematic diagram of the ball-on-plane contact: (a) the geometry of the sample and counter-body; (b) surface morphology of the sample.

Fig. 1 gives the SEM image of the virginal microstructure, which shows a dual phase (α+β) microstructure in which α phase of a dominant globular morphology is homogeneously distributed in β matrix. In order to guide the heat treatment parameter setting, the β-transus temperature of this alloy evaluated by the DIL805 thermal dilatometer with 10 °C/s heating rate is 795±5 °C. On the basis of the examined β-transus temperature, the microstructures with different α morphologies were obtained by three different heat treatment routes, as shown in Fig. 2, i.e., the α+β phase field heat treatment, the β+(α+β) phase field heat treatment and the β+quenching+(α+β) phase field heat treatment. The detailed heat treatments are described below:

1) Heat treatment 1(HT1): α+β phase field heat treatment, isothermal heat treatment at 700 °C in α+β phase field for holding 30 mins followed by water quenching.

2) Heat treatment 2(HT2): β+(α+β) phase field heat treatment, solution treatment at 900 °C in β phase field for holding 30 mins, subsequently annealing at 650 °C for 30 mins followed by water quenching.

3) Heat treatment 3(HT3): β+Quenching+(α+β) phase field heat treatment, solution treatment at 900 °C in β phase field for holding 30 mins followed by water quenching, and then re-heating up to 750 °C for 30 mins followed by water quenching.

All heat treatments above were carried out by using a SG-XQL-1400 muffle furnace with an argon atmosphere protection. The accuracy of temperature control is within ±5 °C.

2.2. Mechanical properties

The micro-hardness of samples was determined by an average value of ten measurements, which were obtained through Vickers hardness test under a normal load of 2 N and a holding time of 15 s. Dog-bone shaped specimens for tensile test following the ASTM-E8 standard with a gauge length of 25 mm, a width of 6 mm and a thickness of 2 mm were prepared by electric discharge machining (EDM). The uniaxial tensile tests were conducted on a CMT5305 hydraulic universal testing machine with an electronic extensometer and a strain rate of 10^{-3}/s. The tensile tests were repeated three times for each sample.

2.3. Fretting wear tests

The fretting wear tests were conducted with a high precision fretting wear test rig self-designed at room temperature, as state in Ref. [6]. In the experimental setup, the relative displacement driven by a piezoelectric ceramic actuator was measured with a grating displacement sensor. The precision of displacement control can be achieved within ±0.1μm. Given that the contact surface of each material is not ideally smooth, but is relatively rough and has lots of micro-asperities on the surface, two bodies contact is more like the ball-on-plane contact configuration in micro-scale. In the current study, therefore, a ball-on-plane contact configuration was chosen for the contact geometry to conduct the fretting wear test as reported in previous study [55], as seen in Fig. 3. In the experimental setup, the samples of a rectangular shape with the size of 15 mm×10 mm×2.5 mm for fretting wear test were mechanically polished following a standard metallographic preparation, eventually achieving a surface roughness of 0.03μm, as shown in Fig. 3(b). Moreover, in order to more significantly weaken the effect of counter body damage regarding to the modification of contact interface and debris formation due to fretting wear, a Si_3N_4 ball with a diameter of 10 mm was employed in favor of an as high as possible hardness as the counter body, and the surface roughness of Ra was 0.05μm. All the fretting wear tests were conducted at room temperature (around 25℃) under a relative humidity ranging from 50 % to 60 % in the local region. In order to assure that the maximum Hertz contact stress in a given load is over the ultimate tensile strength (UTS) for each sample, aiming to observe the fretting wear in relatively harsh condition, in the current study the load condition was applied with 20 N under the various displacement amplitudes, i.e., 1μm, 5μm, 10μm, 20μm, 40μm. Each test was repeated 3 times to make sure the reproducibility of the reported results. The detailed test parameters of fretting wear experiments are shown in Table 2.

Table 2
Fretting wear test parameters.

Test parameters	
Normal load	20 N
Displacement amplitude	1, 5, 10, 20, 40 μm
Frequency	2 Hz
Cycles	10000
Relatively humidity	50 %–60 %

2.4. Microstructure characterization analysis

The microstructure, worn surfaces and worn subsurface of each sample were observed by a ZEISS Sigma 300 scanning electron microscope at a voltage of 5 kV. The three-dimensional morphological of worn scars and wear loss were examined by 3D-white-light interferometer (GTK-16–0295). X-ray diffraction analysis for the determination of microstructural phase of samples before and after fretting wear tests was conducted by Rigaku Rapid IIR with a Cu Kα radiation source at a voltage 40 kV and a current of 250 mA. The energy dispersive spectrometer (EDS) was used to probe the tribo-oxidation on worn scars. Moreover, the top subsurface in the cross section of worn scar was investigated by a focused ion beam (FIB) and transmission electron microscope (TEM) with a model of FEI Tencnai G2 F20 and an accelerating voltage of 200 kV.

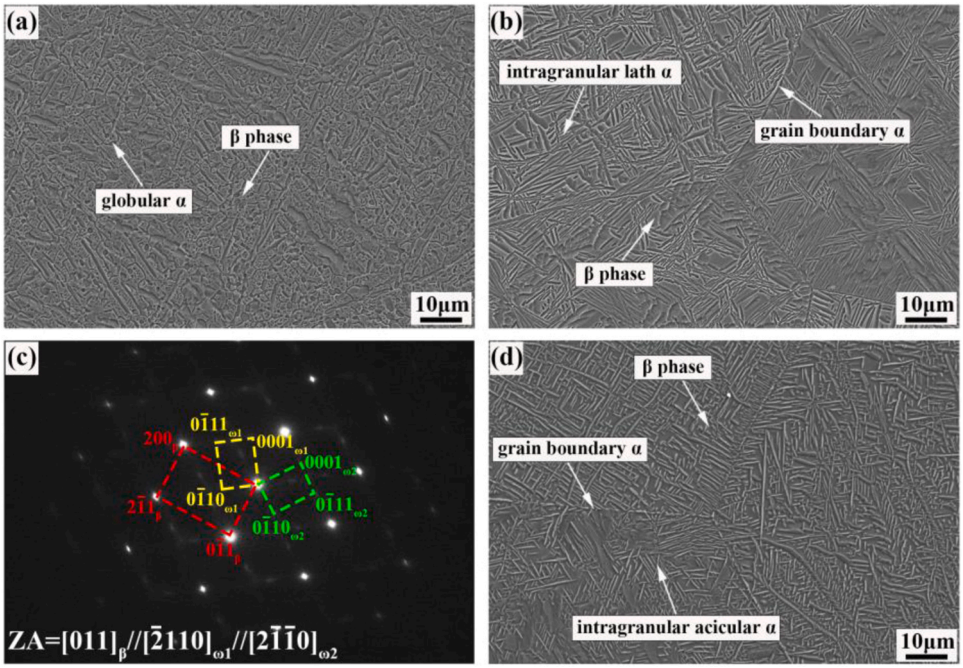

Fig. 4. (a) SEM micrograph of HT1 with globular α, (b) SEM micrograph of HT2 with lath α, (c) SAED patterns of the microstructure prior to intercritical annealing for HT3, and (d) SEM micrograph of HT3 with acicular α.

Table 3
α volume fraction for Ti-10V-2Fe-3Al alloy with different α morphology.

Sample No.	α morphology	Volume fraction
HT1	Globular α	~ 47 %
HT2	Lath α	~ 49 %
HT3	Acicular α	~ 51 %

3. Results

3.1. Microstructures

Fig. 4 displays the SEM micrographs of the rather different microstructures created by three heat treatment. In the α+β phase field treatment route, some α phase in original microstructure was gradually dissolved and transformed to β phase [47]. Due to the low temperature, the morphology of α phase mainly inherited the original globular morphology. As a result, the obtained final microstructure maintains a duplex structure, i.e., globular α phase distributed in β matrix, as shown in Fig. 4(a). While for the β+(α+β) phase field treatment route, the microstructure before entering into the (α+β) phase region is full β phase. Upon lowering the temperature to the (α+β) phase region, the α phase nucleated at the β phase grain boundaries to form primary grain boundary α (α_{GB}), which then grew towards the grains center in a certain direction [56], consequently forming a lath-like α phase distributed in β matrix, as shown in Fig. 4(b). In contrast, for the β+quenching+(α+β) phase field treatment, the starting microstructure prior to intercritical annealing is consisted of a dominant β phase with some homogenous ω phase formed by water quenching from β phase region, as seen in TEM result of Fig. 4(c). Then upon the intercritical annealing treatment, the ω/β interfaces would be prone to promote the formation of acicular α phase by a coupled displacive-diffusional process [57,58]. As a result, the final microstructure is that the acicular α phase involved in the β matrix, as seen in Fig. 4(d). Moreover, in order to separate the effects of the individual parameters (morphology), the volume fraction of α phase in three different samples keeps at the equivalent levels (i.e., 50 %), as shown in Table 3. In order to further reveal the phase structure, the XRD results of the titanium alloys with three different α morphologies are presented in Fig. 5. As can be seen, the samples of different α morphologies all have the peaks of α and β phases, which are consistent with results of SEM images as shown in Fig. 4.

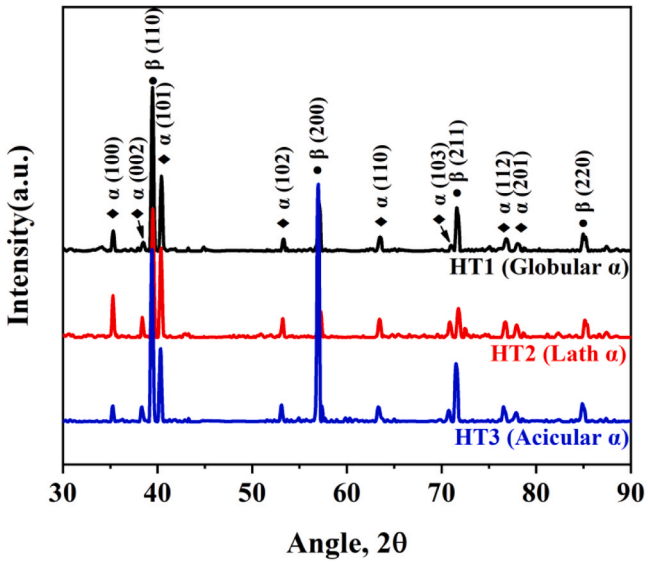

Fig. 5. XRD patterns of the Ti-10V-2Fe-3Al alloy with different α morphology.

3.2. Mechanical properties and hardness

Fig. 6(a) shows the engineering stress-strain curves of the Ti-10V-2Fe-3Al alloy with different α morphologies. It is clear that the three different titanium alloys perform significantly different tensile behaviors, which is strongly dependent on the morphology of α phase. At the same volume fraction of α phase, the sample with acicular α phase has a highest ultimate tensile strength but a lowest uniform elongation. While the sample with lath-like α phase has a largest uniform elongation and a somewhat lowest ultimate tensile strength but the highest hardness, as

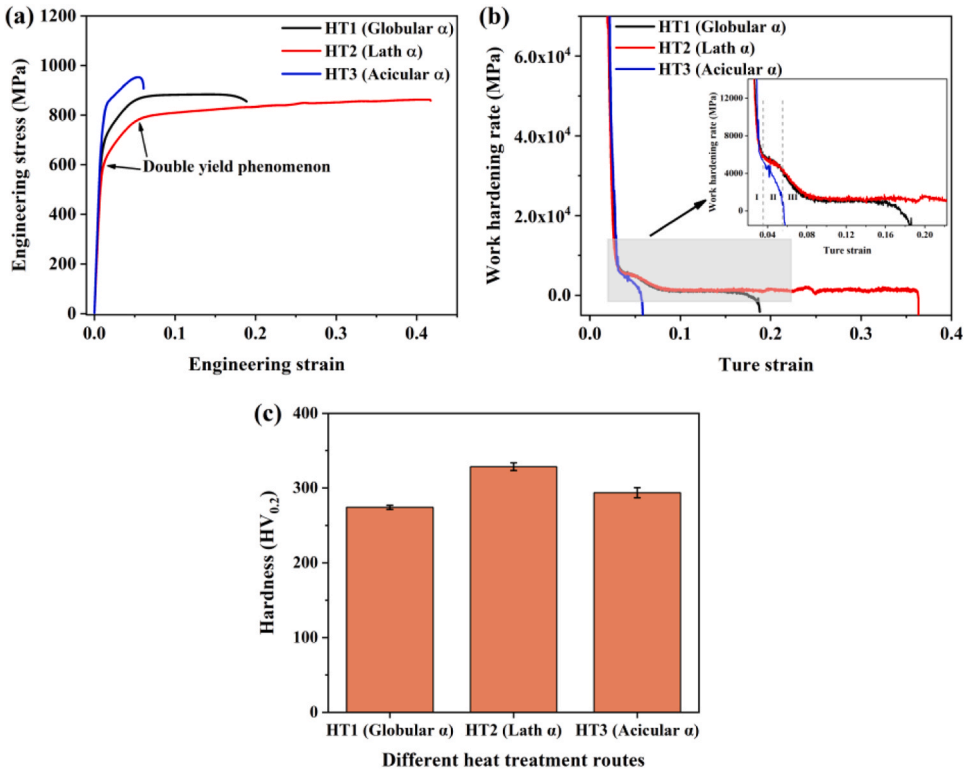

Fig. 6. Mechanical properties of the Ti-10V-2Fe-3Al alloy with different α morphology: (a) Engineering stress-strain curves, (b) Work hardening rate curves, (c) the hardness for each sample.

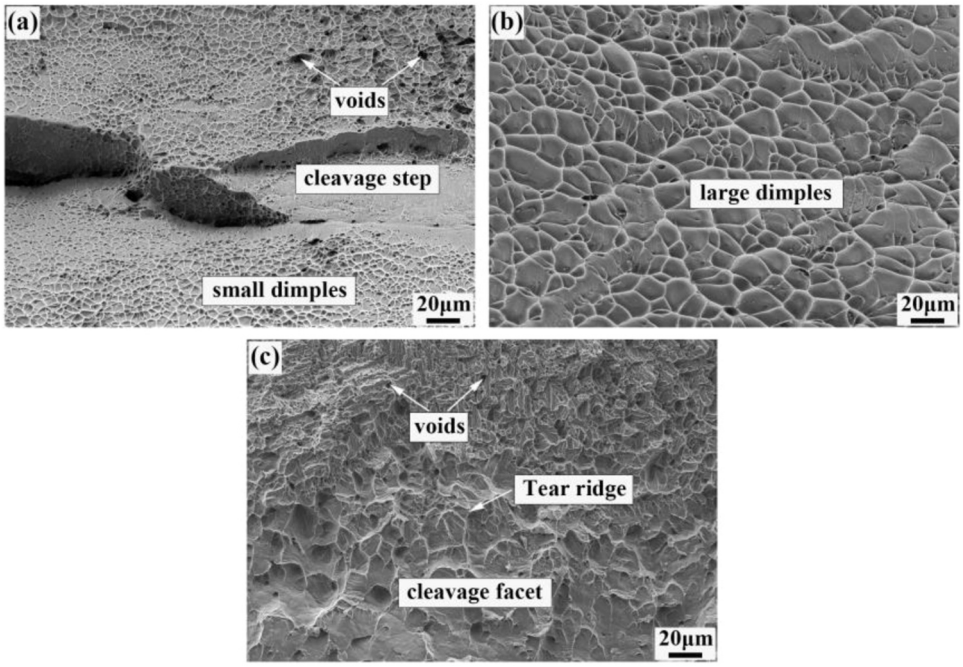

Fig. 7. SEM-fractography of tensile tests for the samples with different α morphology: (a) HT1: globular α, (b) HT2: lath α, (c) HT3: acicular α.

seen in Fig. 6(a and c). In contrast, the sample with the globular α phase has an intermediate ultimate tensile strength and uniform elongation. Furthermore, the stress-strain curves for the samples with globular and lath-like α phase display evident double yield phenomenon as marked in Fig. 6(a). That can be well unraveled by the curve of work hardening rate versus true strain, suggesting a three-stage work hardening behavior with the true strain, as demonstrated in Fig. 6(b). Prior to approaching the first yield point, the work hardening rate rapidly declines as seen in stage I of Fig. 6(b). In the stage II, with the exception of HT3 yielding an acicular α phase, the decrease in work hardening rate of the rest become much slower, which could be associated with the stress induced martensite transformation (SIMT) effect and dislocation pile-up [59,60]. While in the stage III, the decrease of work hardening rate become fast again, which could be the possibility that the contribution

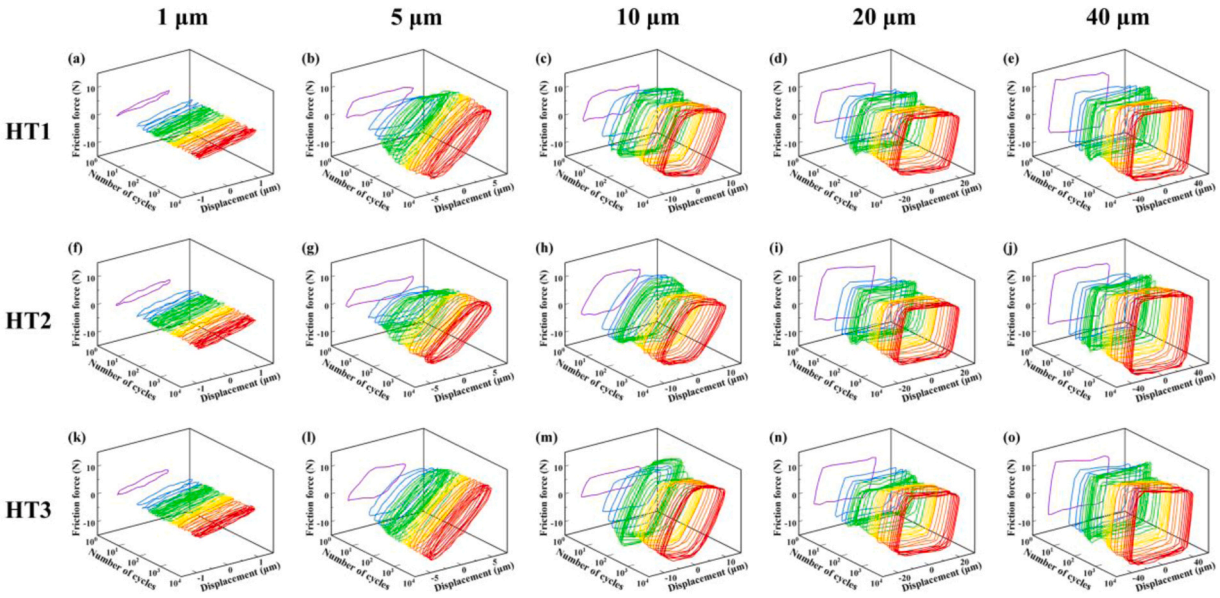

Fig. 8. The evolutions of F_t-D-N curves for the samples with different α morphology subjected to different heat treatment routes.

to the work hardening rate may only arise from dislocation pile-up. It should be noted that for the sample with an acicular α phase, it only presents two stages and shows a comparable level of decrease in work hardening rate to the stage I.

In order to further unravel fracture behavior of the samples with different morphology of α phase, the SEM fractographies of the fractured faces of three different samples are given in Fig. 7. It can be seen that there are lots of small dimples, along with voids and cleavage steps for the sample with globular α phase, which demonstrates that a mixed fracture modes including ductile fracture and cleavage fracture took place. While the dimples become larger and deeper without any cleavage fracture mode for the sample with lath α phase, which could be attributed to the excellent uniform elongation as seen in Fig. 6(a). In contrast, the sample with the acicular α phase nearly presents a quasi-cleavage fracture form including cleavage facet and tear ridge, which could be the result of brittleness nature as shown in Fig. 6(a).

3.3. F_t-D-N curves and the coefficient of friction

Fig. 8 displays the evolutions of the fretting hysteresis loops composed of the varied friction force (F_t) versus displacement amplitude (D) as a function of number of cycles (F_t-D-N curves) under the normal load of 20 N, which may be used to distinguish the fretting regimes of each sample. On the basis of the shape of F_t-D-N curves, three fretting regimes [3,55], i.e., partial slip regime (PSR), mixed fretting regime (MFR) and gross slip regime (GSR), had been clearly observed. As the displacement amplitude is less than 1μm, the F_t-D curves were all shown in the shape of a nearly line at the steady stage as shown in Fig. 8(a), indicating that the fretting wear process was located in partial slip regime. While for the 10μm or even much larger displacement amplitude, all F_t–D curves were open and quasi-rectangular as presented in Fig. 8(c-e), which demonstrates that a relative gross slip took place and the fretting process had run in the GSR. While in the case of an intermediate displacement amplitude such as 5μm, as seen in Fig. 8(b), all F_t–D curves were consisted of elliptical loops at the steady stage referring to the MFR. It should be pointed out that at the beginning stage the F_t-D-N curves for all samples are presented in the elliptical shape (as seen in Fig. 8), which could be the result of surface absorption and oxidation films covered on the specimen surface, as stated in Ref. [4]. In general, under the sample displacement amplitude, all samples were located in the same fretting running regimes, which suggest that the morphology of

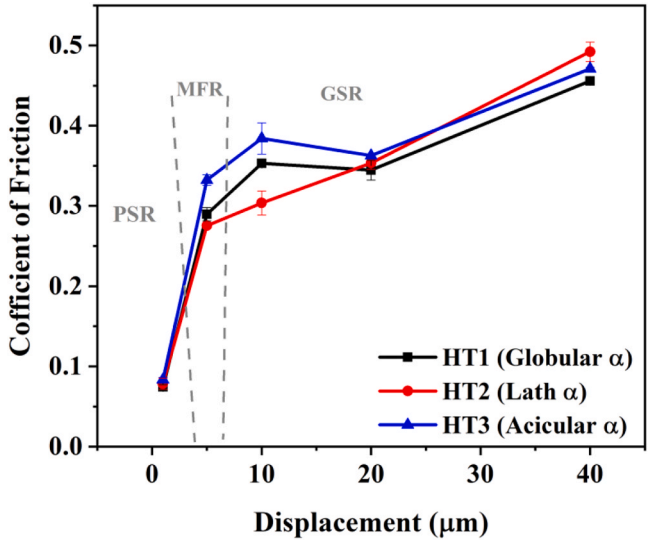

Fig. 9. The coefficient of friction as a function of different displacement amplitudes for the Ti-10V-2Fe-3Al alloy with different α morphology.

α phase play a little effect on the fretting run regime, but influence the friction coefficient depending on the fretting run regimes. Fig. 9 presents the stabilized coefficient of friction (CoF) of the samples with the different morphological α phase as a function of displacement amplitude. Here, it should be noted that the CoF is defined as the ratio between F_t* and F_n, where F_t* is the average value of $F_{t,max}$ and absolute value of ($-F_{t,max}$) for each cycle, and the F_n is the normal load. The stabilized CoF were determined by averaging CoF on the steady state region. It is clear that the equivalent CoFs with quite low value can be observed for all samples in PSR (D = 1μm), which could be ascribed to the existence of the oxidized film and the adsorbates on the initial surface, as well as nearly no relative slip in PSR. With the increase of displacement amplitude to 5μm, i.e., in MFR, the CoFs of samples all increase rapidly, which may due to the removal of pre-oxidized film and the adsorbates on the surface, and the fact that the contact area increases leading to an enhancement of the contact interface adhesion and plastic deformation in MFR. As the displacement further increases up to the GSR, the CoFs approximately continuous to increase, which is associated

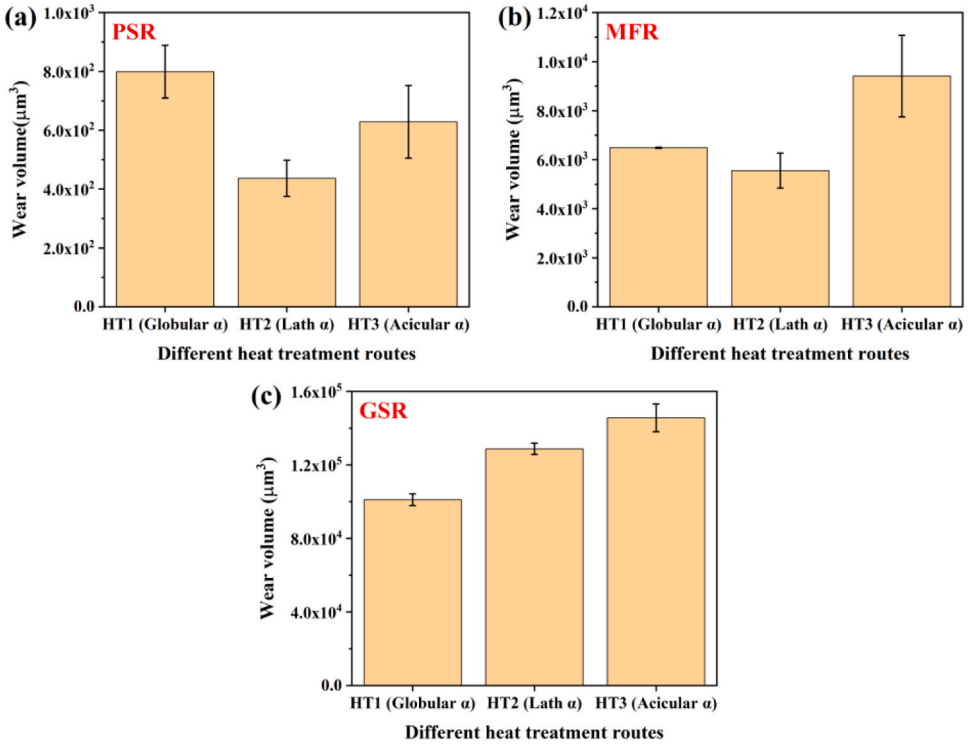

Fig. 10. The fretting wear volume of the microstructures with different α morphology under the three-fretting running regimes.

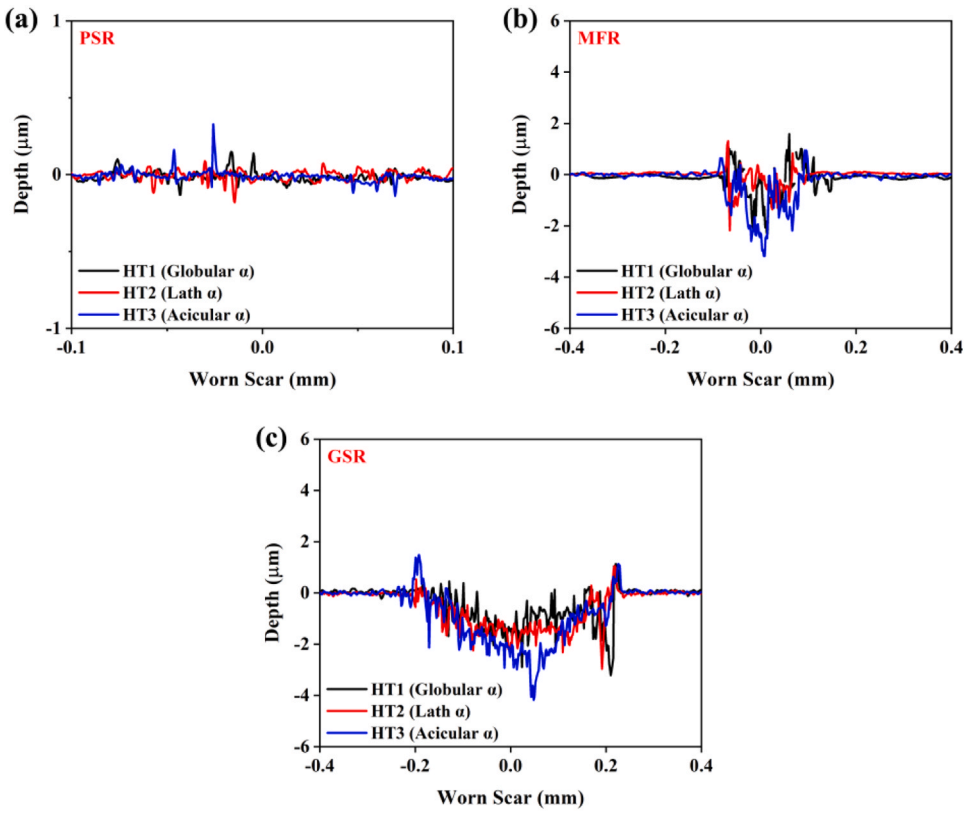

Fig. 11. The two-dimensional profiles of the worn scars of the Ti-10V-2Fe-3Al titanium alloy with different α morphology under the three-fretting running regimes.

to the state of contact interface with respect to the severe plastic deformation and debris formation and as well as the increase of contact area and depth in GSR. Moreover, it can be seen that the HT2 sample with lath α has a lowest CoF in MFR, while in GSR a lowest CoF for the HT1 sample with globular α.

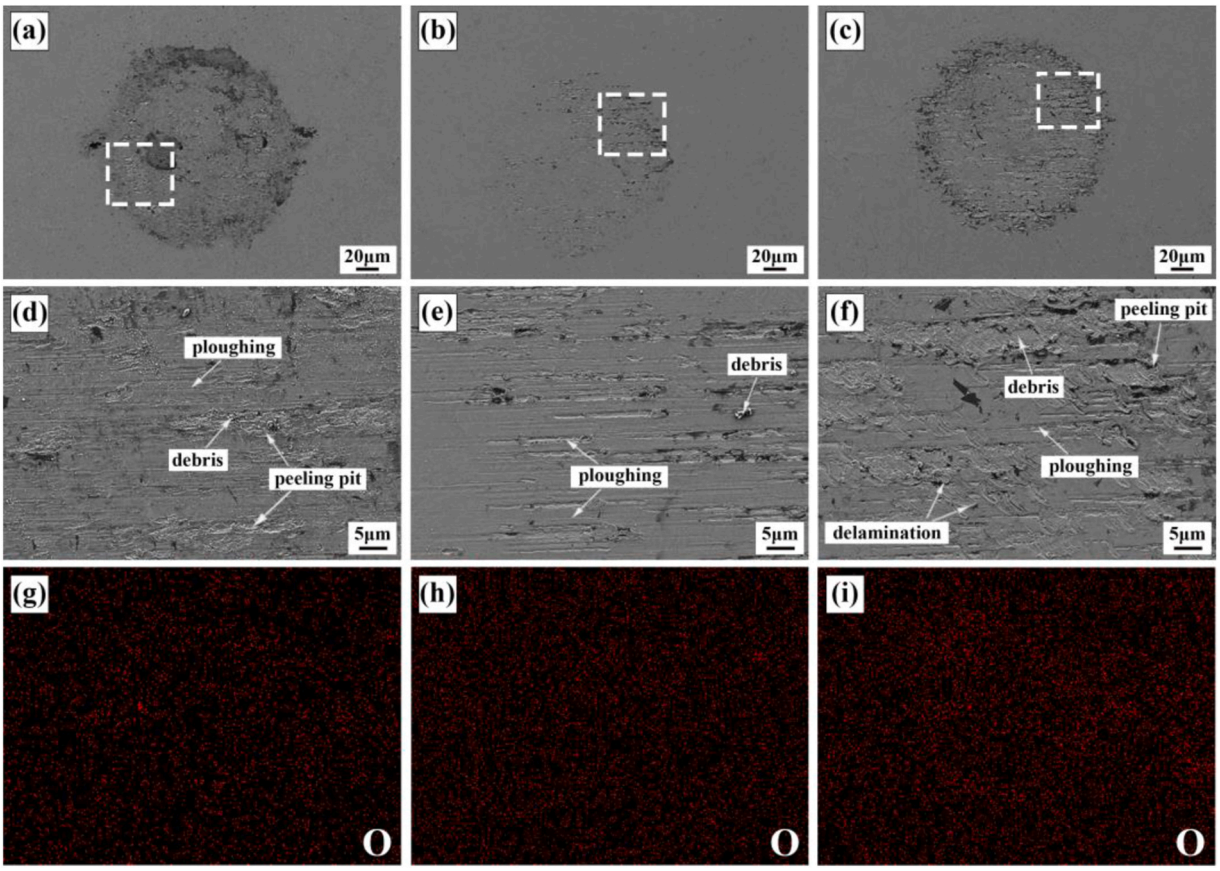

Fig. 12. SEM micrographs and EDS results of the fretting worn scar in the PSR (D=1μm) for all samples: (a, d, g) the sample with globular α; (b, e, h) the sample with lath α; (c, f, i) the sample with acicular α. Note: (d, e, f) are the local magnification of the white square as marked in (a, b, c), respectively.

3.4. Fretting wear volume

The fretting wear volumes for the samples with different α morphology plotted as functions of displacement amplitude are shown in Fig. 10. It can be seen that the α morphology play an important role in determining the fretting wear volume, which depends on the fretting running regimes. In PSR, the HT2 heat treat route to produce the microstructure with lath-like α phase has a lowest wear volume, while the HT1 heat treat route yielding the microstructure with globular α phase has a largest wear volume. Nevertheless, the difference in wear volume among the alloys with different α morphology is not significant in PSR. With the further increase of displacement amplitude entering to the MFR, the microstructure with lath-like α phase still shows a lowest wear volume, but the largest fretting wear volume is the microstructure with acicular α phase rather than that with the globular α phase. While in GSR, it can be noticed that the fretting wear volume follows the order of the microstructure with globular α phase, lath α phase and acicular α phase, i.e., the microstructure with acicular α phase has a largest wear volume, but the lowest wear volume for the microstructure with globular α phase. Moreover, the resulting two-dimensional profiles at the center of the worn scars perpendicular to the sliding direction for all samples under the different fretting running regimes are given in Fig. 11. It is clear that in PSR the profile curves of all samples level off and almost overlap, referring relatively slight wear damage (as seen in Fig. 10a). While for the MFR, the HT3 sample (acicular α phase) shows a largest depth of worn scar, yet the smallest depth of worn scars for the HT2 sample (lath α phase), as shown in Fig. 11(b). In the GSR, the depth of worn scars follows the order of HT1, HT2 and HT3. All results of 2D wear profiles are consistent well with the results shown in Fig. 10.

3.5. Damage observations and wear mechanisms

As the behaviors of the varied displacement amplitudes in GSR were comparable with 40μm being more discriminative, samples produced in GSR of 40μm was selected for further morphological investigation also because they are expected to better represents the failure mechanisms occurred in GSR. Figs. 12–14 give the resulting worn scars of the samples with three different morphological α phases in PSR (D=1μm), MFR (D=5μm), GSR (D=40μm), respectively. It should be noted that the worn scars presented in Figs. 12(d-f)-14(d-f) are resulting local magnified images of Figs. 12(a-c)-14(a-c), respectively. Moreover, the EDS results are also given to probe the surface oxidation of worn scars for all samples under different running regimes, as displayed in Figs. 12(g-i)-14(g-i) respectively.

Fig. 12 illustrates the damage mechanism of the samples in PSR. On the basis of the Mindlin's theory [61], the imposed displacement was mainly accommodated by elastic deformation in PSR, and the distribution of Hertz contact pressure leads to the stick of the center contact zone and the wear annulus around the edge of worn scar. As a result, a micro-slip can be observed as seen in Fig. 12. In contrast, the microstructure with lath-like α phases has no visible fretting wear annulus, showing a very slight fretting wear damage. While for the microstructure with globular and acicular α phases, they both show a comparable level of wear damage with an evident fretting wear annulus, as displayed in Fig. 12(a, c). The local magnified SEM images of the contact zone for all samples reveal that the mechanisms are mainly ploughing, along with some debris for the microstructure with globular and acicular α phases. Meanwhile, the EDS results in Fig. 12(g-i) show that there is no evident tribo-oxidation on the worn scar in PSR, which further implies the marginal fretting damage. The damage observations of worn scars are in good agreement with the resulting wear volume as shown in

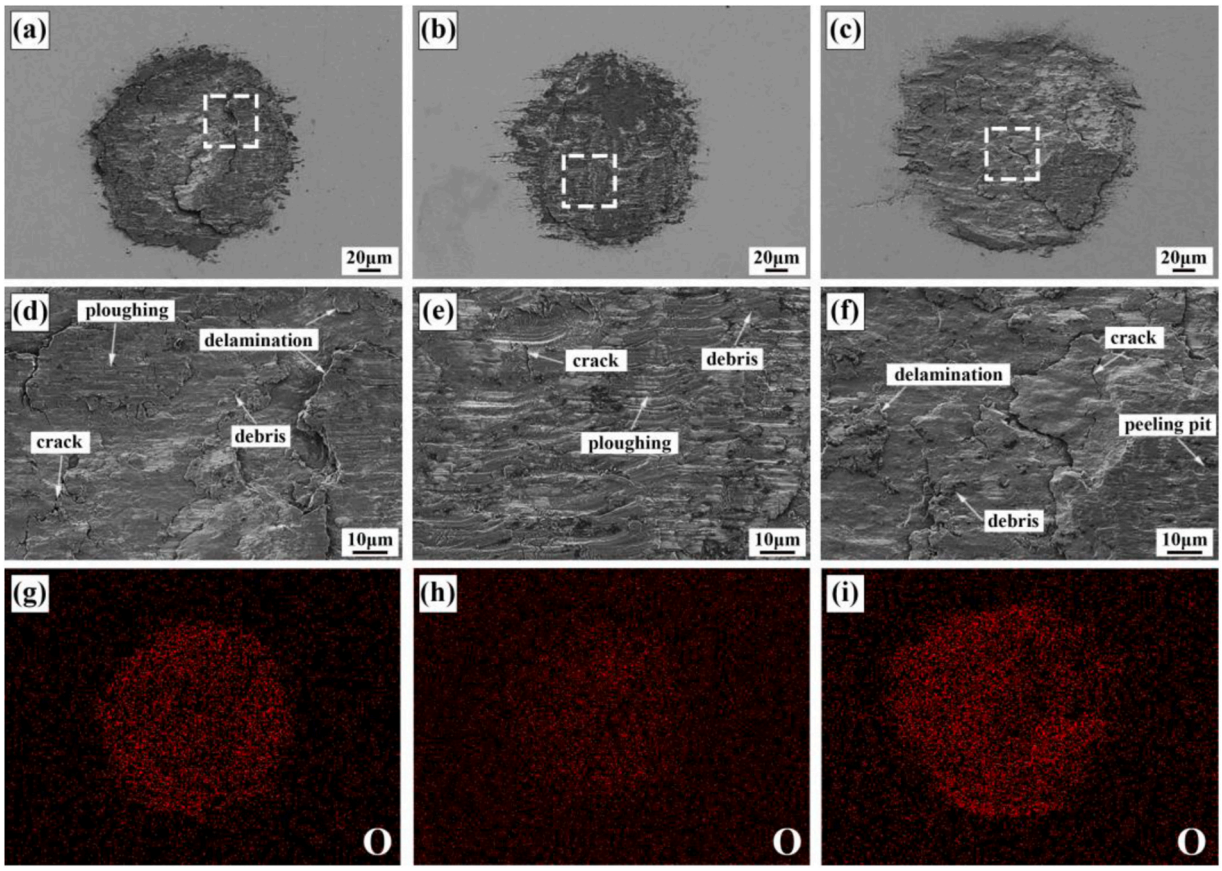

Fig. 13. SEM micrographs and EDS results of the fretting worn scar in the MFR (D=5μm) for all samples: (a, d, g) the sample with globular α; (b, e, h) the sample with lath α; (c, f, i) the sample with acicular α. Note: (d, e, f) are the local magnification of the white square as marked in (a, b, c), respectively.

Fig. 10(a).

With the increase of displacement amplitude entering the MFR, the worn scars and the EDS results of all samples were given in Fig. 13. It can be seen that, as the fretting wear ran in the MFR, the fretting wear damage became more server without the central sticking region, and an evident tribo-oxidation took place on the worn scars, as shown in Fig. 13 (g-i). In comparison among three samples with respect to the area of worn scars and the tribo-oxidation, it follows the order of the microstructure with lath α phase (HT2), globular α phase (HT1) and acicular α phase (HT3), which is consistent with the results of Fig. 10. For the microstructure with the lath-like α phase, the failure mechanism is mainly ploughing accompanied by some cracks and debris formation. In contrast, for the rest severe delamination takes place along with evident cracks and debris as well as tribo-oxidation, especially for the microstructure having the acicular α phase, consequently leading to a highest wear loss.

As the fretting wear ran to GSR (i.e., D=40μm), the worn scars of all microstructures show evident ploughing with different degree of delamination and cracks formed. The microstructure with globular α phase performs a slightest delamination damage, while the microstructure with acicular α phase show a most serious delamination damage, which could be associated with its brittleness nature (as seen in Fig. 6a). Furthermore, the EDS results indicate that the distribution of the O element on the worn scar is consistent with the shape of worn scars as seen in Fig. 14(g-i), which suggest that serious oxidation took place on the worn scars in GSR. The wear damage and tribo-oxidation follow the order of the microstructure with globular α phase (HT1), lath α phase (HT2) and acicular α phase (HT3), which is in line with results shown in Fig. 10(c). In particular with the HT3 sample, the dark region of worn scar in the EDS image implies the oxidized layer delamination, as can also be seen in Fig. 14(c). The results suggest that the morphology of α phase plays an important role in determining the wear damage mechanism depending on the fretting run regimes.

4. Discussions

4.1. *Effect of α morphology*

As stated earlier, α phase plays a significant influence in determining the mechanical properties of metastable β titanium alloys, including the wear resistance. Therefore, there will be two major factors in term of α phase which can affect the fretting wear for the β titanium alloys: 1) the volume fraction of α phase, 2) the morphology, as reported in the previous investigations on dual phase microstructures [62,63]. In order to separate the effect of volume fraction from that of morphology, in the current investigations the volume faction of α phase in the microstructures with different morphologies was fixed at the same level (i.e., ~50 %) so as to well highlight the effect of α phase morphology. Given that in PSR the displacements were mainly accommodated by elastic deformation of contact surface and in MFR it was mainly complies with elastic-plastic deformation [4,64], a good plasticity of microstructure could well impart a super deformation accommodation and absorb the deformation energy, which consequently could improve the fretting wear resistance in PSR and MFR. For the microstructures with globular α phase and lath α phase, they both have better plasticity (as seen in Fig. 6a) and the lath α phase microstructure has a highest hardness (resisting penetration of indenter) as shown in Fig. 6(c). As a result, the lath α phase microstructure has a lowest wear volume (as seen in Fig. 10), while a higher wear volume for the microstructures with globular α phase and acicular α phase. In contrast, as the fretting run to the GSR, the acicular α phase microstructure remains the highest wear volume due to the brittleness nature. While the globular α phase

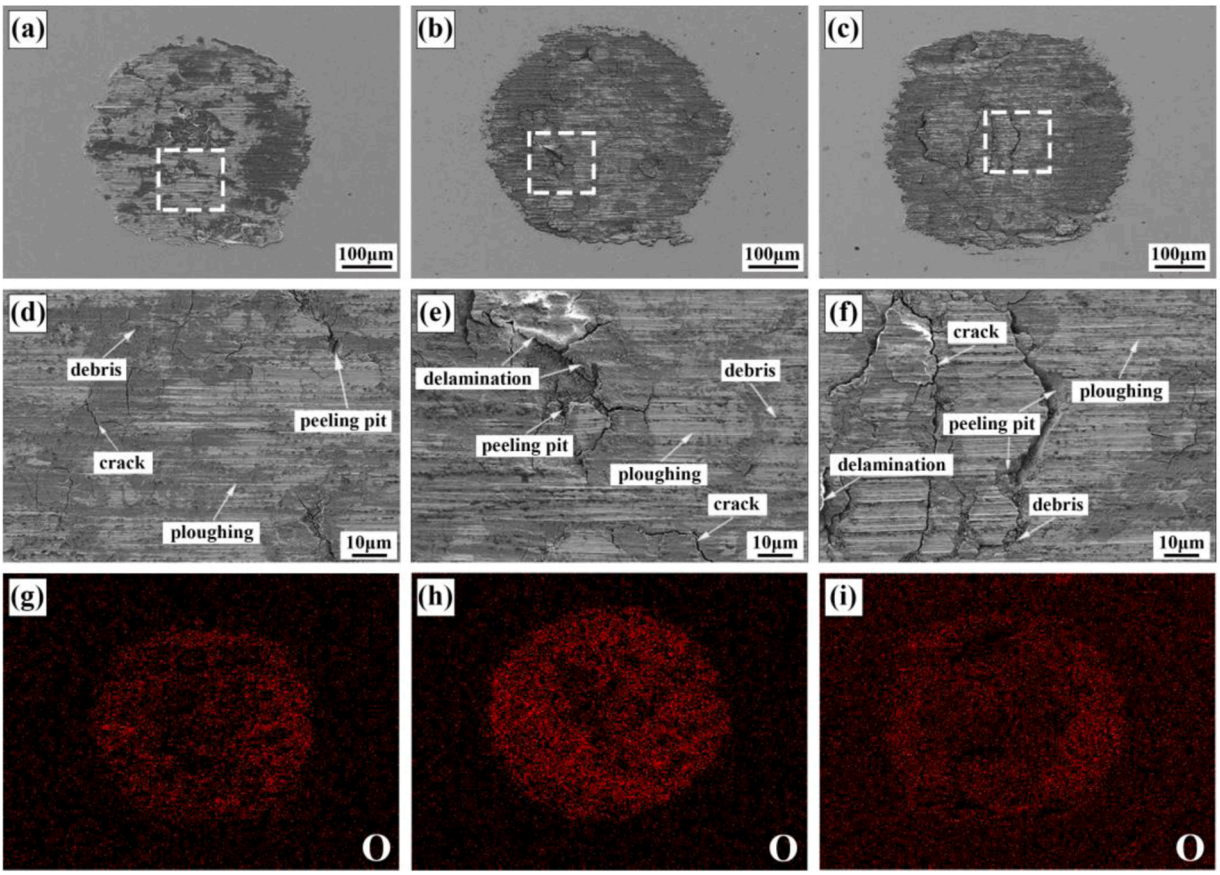

Fig. 14. SEM micrographs and EDS results of the fretting worn scar in the GSR (D=40μm) for all samples: (a, d, g) the sample with globular α; (b, e, h) the sample with lath α; (c, f, i) the sample with acicular α. Note: (d, e, f) are the local magnification of the white square as marked in (a, b, c), respectively.

microstructure has a lowest wear volume, which could be due to the possibility of a good combination of strength and ductility (seen in Fig. 6a), and the stress induced martensite transformation (SIMT) effect for the metastable β titanium which will be discussed next.

In generally, the SIMT can well improve the mechanical properties of metastable β titanium alloy [50,65,66], which can also be applied for enhancing wear resistance. In order to unravel the SIMT effect of the microstructure with different α morphology types during fretting wear process on the fretting wear resistance, a micro-area XRD test was done on the fretting worn scars for each sample under different fretting running regimes. The XRD patterns are shown in Fig. 15(a-c). Besides the α" (021) peak appeared in the microstructure of various α morphology for each fretting running regimes, there are other α" variants, such as α" (110), α" (200), α" (130) and α" (222). Considering the overlap of partial α" peak and α peak in the XRD pattern, the content of α" martensite formed on the worn scars in the current study was estimated by the reduction in content of β phase before and after fretting wear. The volume fraction of the α" martensite for each sample under three fretting running regimes are summarized in Fig. 15(d). It can be seen that, with the increased degree of plastic deformation from PSR to GSR, the α" martensite fraction levels present rising tendency for each morphology type microstructure. In PSR, due to the very small displacement, the comparable levels of α" martensite fraction formed are very low, which could perform with very weak SIMT effects. With increasing the displacement to enter the MFR, both of globular α and lath α microstructure have comparable levels of α" martensite volume fraction, yet which is larger than that of acicular α microstructure. This is consistent with the works reported by Li, et al. [47] and Grosdidier, et al. [67] showed that globular α acted more significantly on β stability than acicular α, and more easily trigger SIMT hence resulting in more α" martensite formed. As stated in [3,4,68], in MFR the crack initiation and propagation is prone to be formed due to elastic-plastic deformation depending on the threshold stress intensity factor ΔK_{th}(resisting the crack propagation) which is consisted of ΔK^{i}_{th}(material interior resistance against crack propagation) and ΔK^{e}_{th}(exterior resistance related to crack path). According to Sun and Paradkar's analysis [68,69], SIMT effect on crack deviation can improve the ΔK^{e}_{th}. Therefore, the microstructures of globular α and lath α morphology type can perform with higher threshold stress intensity factor due to the stronger SIMT effect from more α" martensite fraction (seen in Fig. 15d), consequently leading to the improvement of fretting wear resistance, as shown in Fig. 10(b). In analogy to GSR, given that the microstructure with globular α morphology has a highest α" martensite fraction (i.e., strongest SIMT effect) formed on the worn scars, it presents a best fretting wear resistance. In contrast, the microstructure of acicular α morphology type having the least α" martensite fraction (i.e., weakest SIMT effect) perform a worst resistance to fretting wear.

Moreover, the α morphology in titanium microstructure also can affect the load transfer or stress/strain partitioning between α and β phase during plastic deformation, and hence influences the mechanical properties [70–72], which certainly influences the wear behaviors as well. Especially for GSR, the surface material due to fretting wear would suffer severe plastic deformation. On the basis of Kim's result [71], it is commented that the globular morphology type is harder to deform plastically than the lath/acicular morphology type in dual phase microstructure. Therefore, upon the fretting wear the plastic deformation initiates and develops maximally in the relatively soft β phase but is constrained by the adjacent α phase. The harder deformation response of the globular α phase will in turn cause large misfit strains between α phase and β phase and hence result in a build-up of large stress

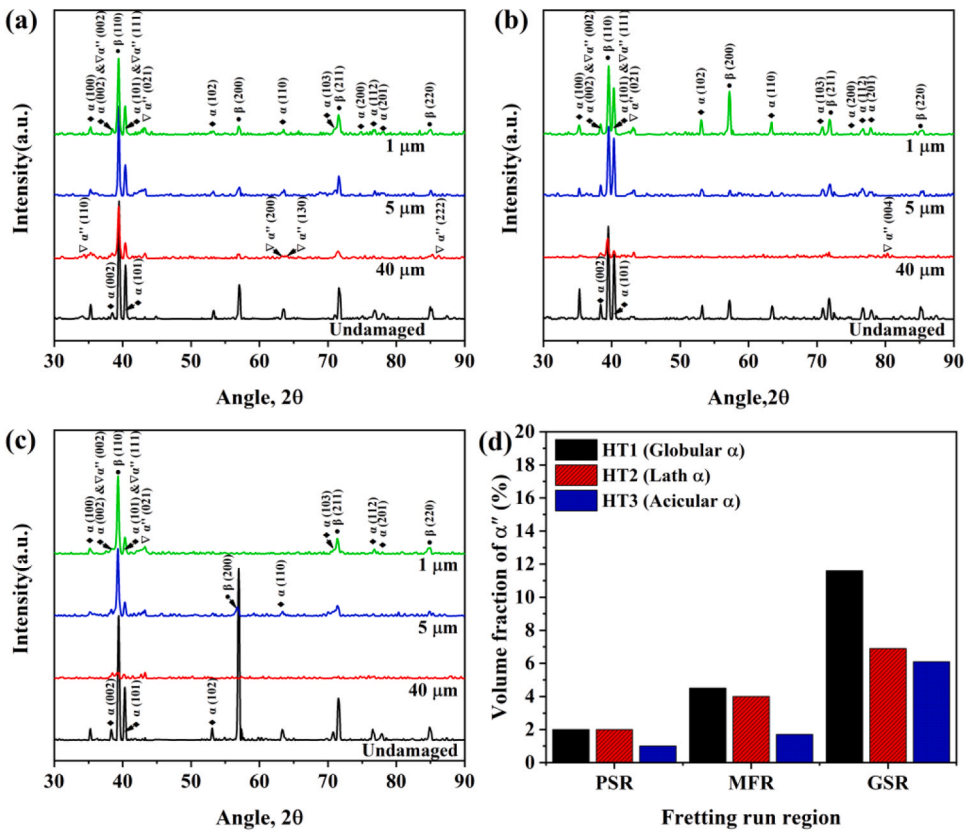

Fig. 15. XRD patterns of the fretting worn scar and original surface for each α morphology type: (a) globular α, (b) lath α, (c) acicular α, and (d) the volume fraction of α" martensite under three fretting running regimes.

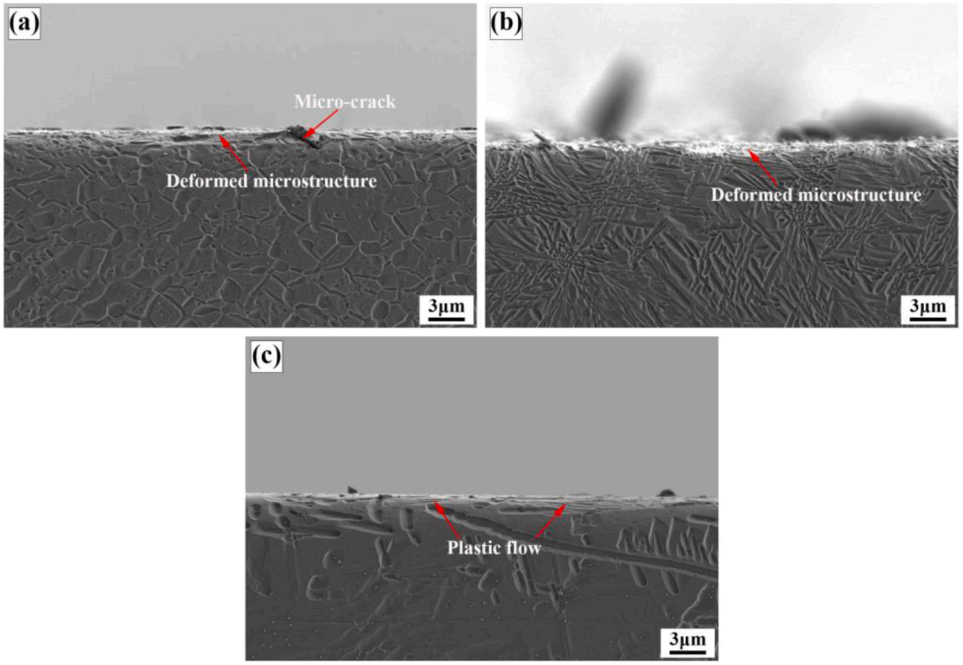

Fig. 16. SEM micrographs of subsurface for different α morphology at PSR (D=1μm): (a) globular α; (b) lath α; (c) acicular α.

concentration. This will further strengthen the α/β interface, dislocation pileup and SIMT effect in globular α phase microstructure. In addition, the multiple α" variants have self-regulating characteristics under local micro-stress constraints which could be helpful to explore the potential for coordinated deformation so as to delay materials damage [73]. As a result, combining these coupled effects above, the globular α phase titanium microstructure (HT1 treated sample) has a lower wear volume than that of the lath and acicular α phase titanium microstructure (HT2 and HT3 treated sample).

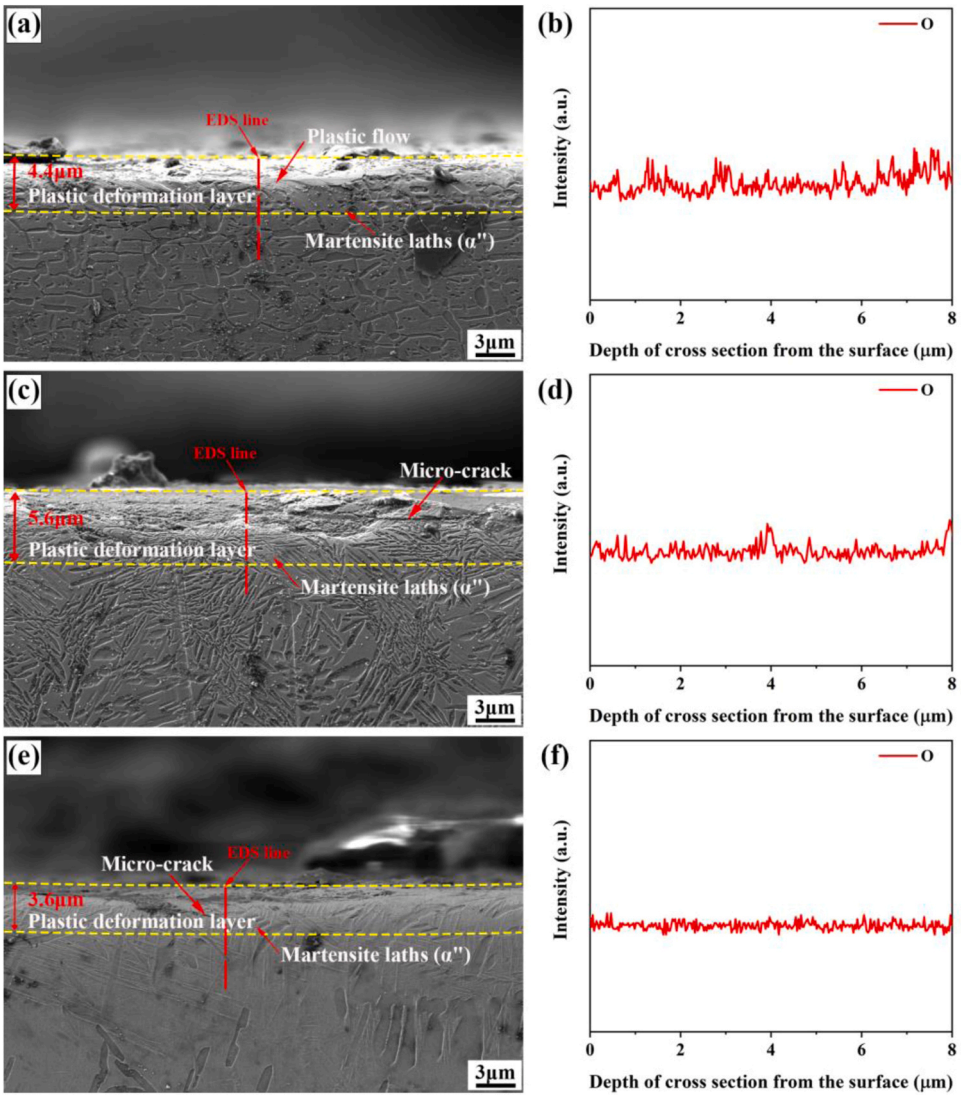

Fig. 17. SEM micrographs and EDS results of subsurface for all samples at MFR (D=5μm): (a, b) globular α, (c, d) lath α, (e, f) acicular α. Note: (b, d, f) are the EDS line scan results of O element from the surface to substrate in the cross section as marked in (a, c, e), respectively.

4.2. The response of the subsurface layer

To understand the response of microstructure beneath the surface upon fretting wear, the microstructural evolutions of the cross-sections parallel to sliding direction for each sample under different fretting running regimes were investigated by SEM, as shown in Figs. 16–18. For all micrographs it is clear that the microstructure beneath the surface was modified with different thickness of subsurface depending on the α microstructures and the fretting running regimes. Fig. 16 displays the SEM micrographs of subsurface for all samples in PSR (D=1μm). It could be found that there is no evident plastic deformation layer on the subsurface layer, but instead only the deformed microstructure/plastic flow on the top surface for all samples as well as the occurrence of micro-cracks for the HT1, which could be attribute to nearly no relative slip on the contact interface during the fretting wear process in PSR. While in MFR (D=5μm), it could be clearly observed that there are obvious plastic deformation layers and martensite laths α" formed for all samples, as shown in Fig. 17. As discussed above, the globular α phase is relatively difficult to be deformed plastically, consequently leading to a relatively low thickness of plastic deformation layer and showing an evident plastic flow due to ploughing. While for the acicular α morphology, because of its worst ductility and brittleness nature (as seen in Fig. 6a and Fig. 7c) and hence serious delamination occurred (as shown in Fig. 13f), it displays a lowest thickness of deformation layer accompanied with micro-crack. In contrast, given the super ductility of the lath α morphology type, it shows a thickest plastic deformation layer, which can well protect the surface against the fretting wear hence resulting in a lowest wear volume in MFR.

Fig. 18 gives the SEM micrographs of subsurface for different α morphology microstructure in GSR (D=40μm). In comparison to MFR, the plastic deformation layer become more compacted and its thickness become larger in GSR due to severe plastic deformation. It can be seen that the acicular α morphology microstructure still performs with a lowest thickness of deformation layer (seen in Fig. 18e-f), hence showing a highest wear volume. While the microstructure of lath α morphology has a relatively compacted and larger thickness of deformation as seen in Fig. 18c-d, which could be the cause of lower wear volume than that of acicular α morphology microstructure. In contrast, for the microstructure with the globular α morphology, a clearly visible mechanical mixture layer (MML) was generated on the top of the subsurface, which may be attributed to the possibility of the large misfit strains and the build-up of large stress concentration due to the difficult-to-deform response of the globular α phase as stated above. Meanwhile, with the exception of PSR having no evident subsurface due to the slight damage, the EDS line scan analysis in the cross section of worn scars from the top surface to substrate was also done to probe the subsurface oxidation for

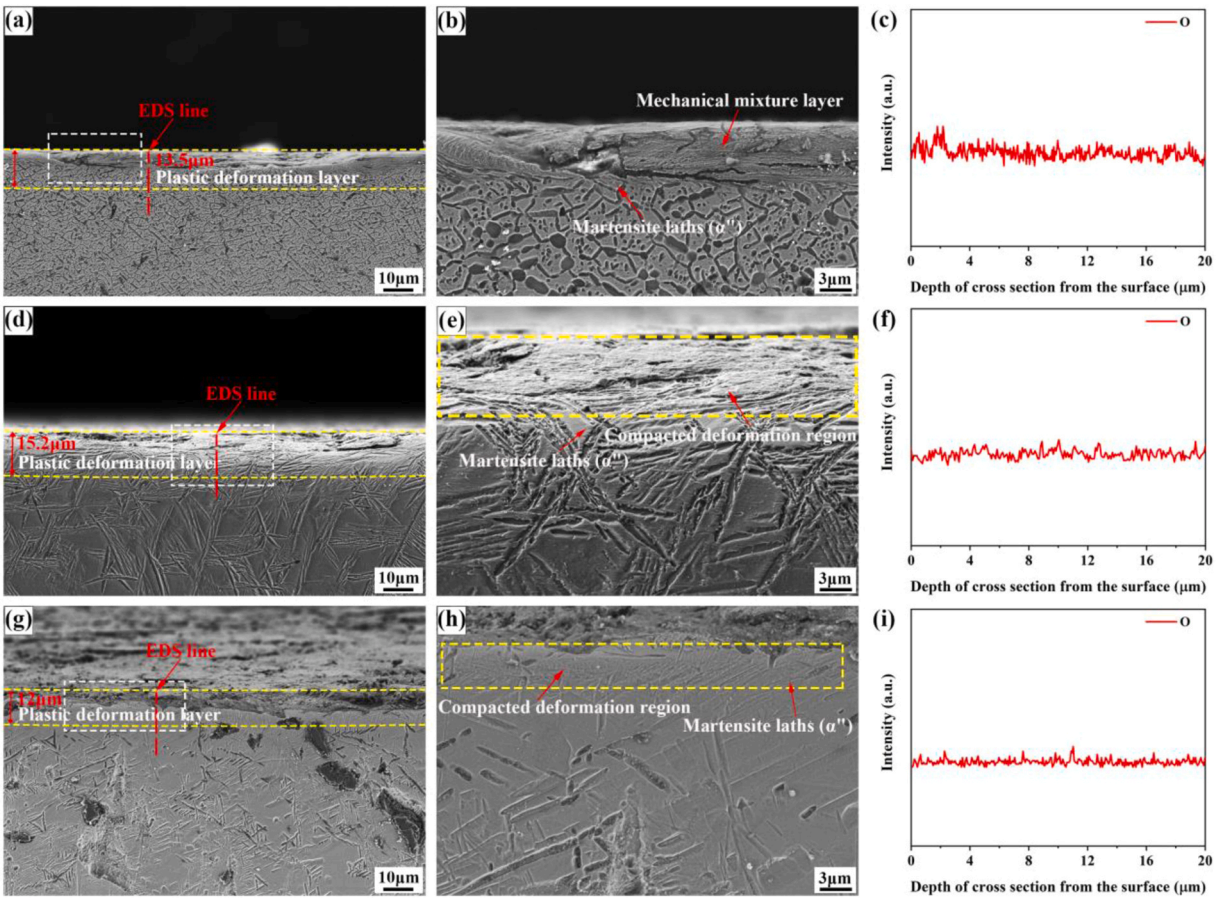

Fig. 18. SEM micrographs and EDS results of subsurface for all samples at GSR (D=40μm): (a, b, c) the sample with globular α; (d, e, f) the sample with lath α; (g, h, i) the sample with acicular α. Note: (b, e, h) are the local magnification of the white square as marked in (a, d, g), and (c, f, i) are the EDS line scan results of O element from the surface to substrate in the cross section as marked in (a, d, g), respectively.

MFR and GSR, as shown in Fig. 17 (b, d, f) and Fig. 18(c, f, i). It can be observed that there is no apparent change in the distribution of O element along the depth direction, which may demonstrate that the tribo-oxidized layer on the top subsurface is very thin for all samples and hence is difficult to be revealed.

Moreover, in order to further distinguish the stress-induced martensite transformation, the highest wear resistant HT1 sample in GSR was selected for further investigated. FIB was used to sample the top subsurface layer of worn scar in the cross section (seen in Fig. 19a), and resulting TEM images are shown in Fig. 19(b-d). It is clear that the top subsurface (MML) layer is mainly consisted of nanocrystals due to severe plastic deformation during fretting wear. Meanwhile, the fast Fourier transform (FFT) was performed on the selected area marked by the square in Fig. 19(c). The diffraction patterns in the FFT image of Fig. 19 (d) reveal the formation of α" martensite, as reported in Ref. [74]. The FFT image well proves the occurrence of stress-induced martensite transformation in MML layer, as displayed in the results of micro-area XRD in Fig. 15a and SEM images of subsurface in Fig. 18(b). As stated by Li et al. [75], the MML would play an effective protection role against wear and then improve the wear resistance during wear process. Therefore, the microstructure having a globular α morphology can perform with a highest fretting wear resistant, which is consistent with the result of Fig. 10(c).

5. Conclusions

This paper presents an experimental investigation on the fretting wear behavior of a Ti-10V-2Fe-3Al titanium alloy heat treated to create α+β dual phase microstructures with three different α morphology, i.e., globular α morphology, lath α morphology and acicular α morphology. Results show that the α morphology has a significant influence on fretting wear behaviors depending on the fretting run regimes. On the basis of the experimental observations, the following conclusions can be draw:

(1) The microstructures with globular and lath α morphology has a good combination of strength and ductility, while the acicular α morphology microstructure has lowest ductility showing a brittleness nature.

(2) In the PSR and MFR, the microstructure with lath α morphology has a lowest fretting wear volume. While in GSR, the microstructure with globular α morphology has a lowest fretting wear volume showing a best performance against fretting wear, yet the worst fretting wear resistance for the acicular α type microstructure.

(3) SIMT effect due to fretting wear plays a positive role in improving fretting wear resistance depending on the α morphology and fretting run regimes. In PSR, the SIMT effect is very weak due to the marginal α" martensite fraction. While in the MFR, comparable levels of α" martensite fraction for both globular α and lath α microstructure are larger than that of acicular α microstructure. In contrast, in GSR the globular α microstructure has a highest α" martensite fraction and hence strongest SIMT effect.

(4) Subsurface analysis demonstrates that a compacted and thick plastic deformation layer, especially the mechanical mixture layer, can well protect the material surface against fretting wear.

Funding

This work was supported by the Natural Science Foundation of China

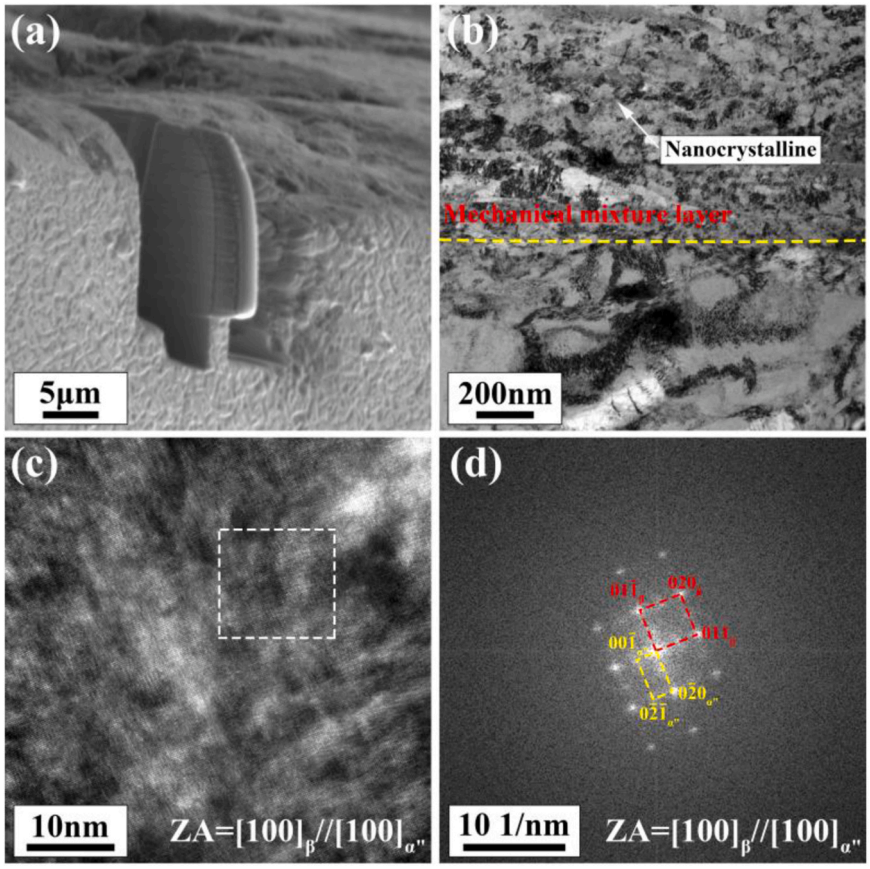

Fig. 19. TEM images of subsurface for the microstructure with globular α morphology in GSR: (a) the sampling position in the top subsurface of worn scar; (b) the bright-field image; (c) the high-resolution image viewed along [100] zone axis in the mechanical mixture layer of (c); (d) the FFT image. (Note: the FFT area is marked by the square in (c)).

(52171079) and Sichuan Science and Technology Program (2023NSFSC0413).

CRediT authorship contribution statement

Xiaojun Xu: Writing – review & editing, Supervision, Methodology, Funding acquisition, Conceptualization. **Xiage Zhang:** Investigation, Formal analysis. **Jianjun Long:** Writing – review & editing, Writing – original draft, Methodology, Investigation, Conceptualization. **Binbin Gan:** Writing – review & editing. **Yiting Dong:** Writing – review & editing, Formal analysis. **Minhao Zhu:** Supervision, Funding acquisition. **Hao Li:** Methodology, Formal analysis.

Declaration of Competing Interest

The authors declare that they have no known competing financial interests or personal relationships that could have appeared to influence the work reported in this paper.

Acknowledgment

The authors gratefully acknowledge financial supported by the Natural Science Foundation of China (52171079), and supported by Sichuan Science and Technology Program (2023NSFSC0413).

Data Availability

Data will be made available on request.

References

[1] L. Vincent, Y. Berthier, M.C. Dubourg, M. Godet, Mechanics and materials in fretting, Wear 153 (1992) 135–148, https://doi.org/10.1016/0043-1648(92)90266-B.
[2] Y.H. Lee, H.K. Kim, Fretting wear behavior of a nuclear fuel rod under a simulated primary coolant condition, Wear 301 (2013) 569–574, https://doi.org/10.1016/j.wear.2013.01.067.
[3] Z.R. Zhou, K. Nakazawa, M.H. Zhu, N. Maruyama, P. Kapsa, L. Vincent, Progress in fretting maps, Tribology Int. 39 (2006) 1068–1073, https://doi.org/10.1016/j.triboint.2006.02.001.
[4] M.H. Zhu, Z.R. Zhou, On the mechanisms of various fretting wear modes, Tribology Int. 44 (2011) 1378–1388, https://doi.org/10.1016/j.triboint.2011.02.010.
[5] D. Cressman, B. Tury, G.L. Doll, Effects of surface treatments and coatings on tribological performance of Ti-6Al-4V in the mixed fretting and gross slip regimes, Surf. Coat. Technol. 276 (2015) 260–265, https://doi.org/10.1016/j.surfcoat.2015.06.055.
[6] X. Qiu, X. Wei, X. Xu, W. Xu, M. Zhu, Dependence of fretting wear resistance on microstructural features of alloyed steels, Tribology Int. 137 (2019) 39–45, https://doi.org/10.1016/j.triboint.2019.04.028.
[7] I.I. Argatov, Y.S. Chai, A self-similar model for fretting wear contact with the third body in gross slip, Wear 466-467 (2021) 203562, https://doi.org/10.1016/j.wear.2020.203562.
[8] Y. Yang, C. Wang, Y. Gesang, H. Shang, R. Wang, Y. Liang, T. Wang, Q. Chen, T. Shao, Fretting wear evolution of γ-TiAl alloy, Tribology Int. 154 (2021) 106721, https://doi.org/10.1016/j.triboint.2020.106721.
[9] J.F. Matlik, T.N. Farris, F.K. Haake, G.R. Swanson, G.C. Duke, High-frequency, high-temperature fretting-fatigue experiments, Wear 261 (2006) 1367–1382, https://doi.org/10.1016/j.wear.2006.03.048.
[10] P.M. Wavish, D. Houghton, J. Ding, S.B. Leen, E.J. Williams, I.R. McColl, A multiaxial fretting fatigue test for spline coupling contact, Fatigue Fract. Eng. Mater. Struct. 32 (2009) 325–345, https://doi.org/10.1111/j.1460-2695.2009.01334.x.
[11] E. Zalnezhad, G. Faraji, Fretting fatigue life investigation of AL7075-T6 alloy coated by multilayer thin solid films of TiCr/TiN/CrN and Ti/Cr/TiN/Cr/CrN/TiCrN, Proc. Inst. Mech. Eng., Part J: J. Eng. Tribology 231 (2016) 686–692, https://doi.org/10.1177/1350650116672145.

[12] Z.B. Cai, Z.Y. Li, M.G. Yin, M.H. Zhu, Z.R. Zhou, A review of fretting study on nuclear power equipment, Tribology Int. 144 (2020) 106095, https://doi.org/10.1016/j.triboint.2019.106095.

[13] M.H. Attia, A. de Pannemaecker, G. Williams, Effect of temperature on tribo-oxide formation and the fretting wear and friction behavior of zirconium and nickel-based alloys, Wear 476 (2021) 203722, https://doi.org/10.1016/j.wear.2021.203722.

[14] M. Godjevac, T. van Beek, H.T. Grimmelius, T. Tinga, D. Stapersma, Prediction of fretting motion in a controllable pitch propeller during service, Proc. Inst. Mech. Eng., Part M: J. Eng. Marit. Environ. 223 (2009) 541–560, https://doi.org/10.1243/14750902jeme128.

[15] M. Wang, Y. Wang, H. Liu, F. Yan, Effect of load on the fretting behavior of SAF 2507 super duplex stainless steel in air and sea water, Ind. Lubr. Tribology 72 (2019) 651–656, https://doi.org/10.1108/ilt-08-2019-0335.

[16] D. Banerjee, J.C. Williams, Perspectives on titanium science and technology, Acta Mater. 61 (2013) 844–879, https://doi.org/10.1016/j.actamat.2012.10.043.

[17] Z. Tarzimoghadam, S. Sandlöbes, K.G. Pradeep, D. Raabe, Microstructure design and mechanical properties in a near-α Ti–4Mo alloy, Acta Mater. 97 (2015) 291–304, https://doi.org/10.1016/j.actamat.2015.06.043.

[18] Q. Ming, Z. Yong, Y. Jian, Z. Jun, Microstructure and tribological characteristics of Ti-6Al-4V alloy against GCr15 under high speed and dry sliding, Mater. Sci. Eng.: A 434 (2006) 71–75, https://doi.org/10.1016/j.msea.2006.07.043.

[19] A. Molinari, G. Straffelini, B. Tesi, T. Bacci, Dry sliding wear mechanisms of the Ti6Al4V alloy, wear 208 (1997) 105–112, https://doi.org/10.1016/S0043-1648(96)07454-6.

[20] S. Fouvry, P. Duó, P. Perruchaut, A quantitative approach of Ti-6A-4V fretting damage: friction, wear and crack nucleation, Wear 257 (2004) 916–929, https://doi.org/10.1016/j.wear.2004.05.011.

[21] Q. Song, L. Liu, D. Wen, Y. Wang, G. Wang, Z. Yin, S. Wang, Fretting wear behaviors and mechanism of a high NbTiAl alloy with full lamellar microstructure at ambient temperature, J. Mater. Sci. 57 (2022) 15636–15650, https://doi.org/10.1007/s10853-022-07605-x.

[22] J. Pu, Y. Zhang, X. Zhang, X. Zhang, X. Yuan, Z. Wang, G. Zhang, W. Cui, Z. Jin, Revealing the composite fretting-corrosion mechanisms of Ti6Al4V alloy against zirconia-toughened alumina ceramic in simulated body fluid, J. Mech. Behav. Biomed. Mater. 146 (2023) 106074, https://doi.org/10.1016/j.jmbbm.2023.106074.

[23] R.B. Waterhouse, A. Iwabuchi, High temperature fretting wear of four titanium alloys, Wear 106 (1985) 303–313, https://doi.org/10.1016/0043-1648(85)90114-0.

[24] X. Zhang, D. Liu, Effiects of temperature, slip amplitude, contact pressure on fretting fatigue behavior of Ti811 alloys at elevated temperatures, Acta Metall. Sin. (Engl. Lett.) 22 (2009) 131–137, https://doi.org/10.1016/s1006-7191(08)60080-0.

[25] X. Zhang, D. Liu, Investigation of fretting fatigue behavior of Ti811 alloy at elevated temperature, Int. J. Mod. Phys. B 22 (2008) 5489–5494, https://doi.org/10.1142/S021797920805070X.

[26] X. Cheng, X. Wei, H. Li, H. Wei, X. Xu, L. Sheng, M. Zhu, Investigation on the fretting wear behavior of titanium alloy under different atmospheres by an in situ XPS spectrometry, Int. J. Mod. Phys. B 36 (2022) 2250109, https://doi.org/10.1142/s0217979222501090.

[27] C. Mary, T. Le Mogne, B. Beaugiraud, B. Vacher, J.M. Martin, S. Fouvry, Tribochemistry of a Ti alloy under fretting in air: evidence of titanium nitride formation, Tribology Lett. 34 (2009) 211–222, https://doi.org/10.1007/s11249-009-9426-6.

[28] C. Zhang, F. Shen, L. Ke, Electrical contact resistance endurance of AgNi10 alloy under fretting wear: Experiment and numerical prediction, Wear 530-531 (2023) 205009, https://doi.org/10.1016/j.wear.2023.205009.

[29] F. Shen, W. Hu, Q. Meng, A damage mechanics approach to fretting fatigue life prediction with consideration of elastic-plastic damage model and wear, Tribology Int. 82 (2015) 176–190, https://doi.org/10.1016/j.triboint.2014.10.017.

[30] F. Shen, L. Ke, K. Zhou, A debris layer evolution-based model for predicting both fretting wear and fretting fatigue lifetime, Int. J. Fatigue 142 (2021) 105928, https://doi.org/10.1016/j.ijfatigue.2020.105928.

[31] Z.R. Zhou, S.R. Gu, L. Vincent, An investigation of the fretting wear of two aluminium alloys, Tribology Int. 30 (1997) 1–7, https://doi.org/10.1016/0301-679X(95)00118-N.

[32] X. Xu, S. van der Zwaag, W. Xu, The effect of ferrite-martensite morphology on the scratch and abrasive wear behaviour of a dual phase construction steel, Wear 348-349 (2016) 148–157, https://doi.org/10.1016/j.wear.2015.12.005.

[33] X. Xu, S. van der Zwaag, W. Xu, The effect of martensite volume fraction on the scratch and abrasion resistance of a ferrite-martensite dual phase steel, Wear 348-349 (2016) 80–88, https://doi.org/10.1016/j.wear.2015.11.017.

[34] Y. Danard, G. Martin, L. Lilensten, F. Sun, A. Seret, R. Poulain, S. Mantri, R. Guillou, D. Thiaudière, I. Freiherr von Thüngen, D. Galy, M. Piellard, N. Bozzolo, R. Banerjee, F. Prima, Accommodation mechanisms in strain-transformable titanium alloys, Mater. Sci. Eng.: A 819 (2021) 141437, https://doi.org/10.1016/j.msea.2021.141437.

[35] F. Sun, J.Y. Zhang, M. Marteleur, T. Gloriant, P. Vermaut, D. Laillé, P. Castany, C. Curfs, P.J. Jacques, F. Prima, Investigation of early stage deformation mechanisms in a metastable β titanium alloy showing combined twinning-induced plasticity and transformation-induced plasticity effects, Acta Mater. 61 (2013) 6406–6417, https://doi.org/10.1016/j.actamat.2013.07.019.

[36] R.R. Boyer, G.W. Kuhlman, Processing properties relationships of Ti-10V-2Fe-3Al, Metallurgical and, Mater. Trans. A 18 (1987) 2095–2103, https://doi.org/10.1007/BF02647081.

[37] J.O. Peters, G.L. Tjering, Comparison of the fatigue and fracture of α+β and β titanium alloys, Metall. Mater. Trans. A 32 (2001) 2805–2818, https://doi.org/10.1007/s11661-001-1031-8.

[38] T.W. Duerig, J. Albrecht, D. Richter, P. Fischer, Formation and reversion of stress induced martensite in Ti-10V-2Fe-3Al, Acta Metall. 30 (1982) 2161–2172, https://doi.org/10.1016/0001-6160(82)90137-7.

[39] C. Wu, Y. Zhao, S. Huang, L. Lei, Q. Zhao, Q. Sun, L. Zhou, Microstructure tailoring and impact toughness of a newly developed high strength Ti-5Al-3Mo-3V-2Cr-2Zr-1Nb-1Fe alloy, Mater. Charact. 175 (2021) 111103, https://doi.org/10.1016/j.matchar.2021.111103.

[40] W. Zhu, Q. Sun, C. Tan, P. Li, L. Xiao, J. Sun, Tensile brittleness and ductility improvement in a novel metastable β titanium alloy with lamella structure, J. Alloy. Compd. 827 (2020) 154311, https://doi.org/10.1016/j.jallcom.2020.154311.

[41] W. Zhu, J. Lei, C. Tan, Q. Sun, W. Chen, L. Xiao, J. Sun, A novel high-strength β-Ti alloy with hierarchical distribution of α-phase: the superior combination of strength and ductility, Mater. Des. 168 (2019) 107640, https://doi.org/10.1016/j.matdes.2019.107640.

[42] S.W. Lee, J.H. Kim, C.H. Park, J.K. Hong, J.T. Yeom, Alloy design of metastable α+β titanium alloy with high elastic admissible strain, Mater. Sci. Eng.: A 802 (2021) 140621, https://doi.org/10.1016/j.msea.2020.140621.

[43] X. Xu, S. van der Zwaag, W. Xu, A novel multi-pass dual-indenter scratch test to unravel abrasion damage formation in construction steels, Wear 322-323 (2015) 51–60, https://doi.org/10.1016/j.wear.2014.10.011.

[44] X. Xu, S. v.d. Zwaag, W. Xu, Prediction of the abrasion resistance of construction steels on the basis of the subsurface deformation layer in a multi-pass dual-indenter scratch test, Wear, 338- 339 (2015) 47–53, https://doi.org/10.1016/j.wear.2015.05.012.

[45] C. Zhu, X. Zhang, C. Li, C. Liu, K. Zhou, A strengthening strategy for metastable β titanium alloys: Synergy effect of primary α phase and β phase stability, Mater. Sci. Eng.: A 852 (2022) 143736, https://doi.org/10.1016/j.msea.2022.143736.

[46] Y. Fu, W. Xiao, J. Wang, X. Zhao, C. Ma, Mechanical properties and deformation mechanisms of Ti-15Nb-5Zr-4Sn-1Fe alloy with varying α phase fraction, J. Alloy. Compd. 898 (2022) 162816, https://doi.org/10.1016/j.jallcom.2021.162816.

[47] C. Li, X. Wu, J.H. Chen, S. van der Zwaag, Influence of α morphology and volume fraction on the stress-induced martensitic transformation in Ti-10V-2Fe-3Al, Mater. Sci. Eng.: A 528 (2011) 5854–5860, https://doi.org/10.1016/j.msea.2011.03.107.

[48] J. Wang, Y. Zhao, W. Zhou, Q. Zhao, S. Huang, W. Zeng, In-situ investigation on tensile deformation and fracture behaviors of a new metastable β titanium alloy, Mater. Sci. Eng.: A 799 (2021) 140187, https://doi.org/10.1016/j.msea.2020.140187.

[49] F. Niessen, E. Pereloma, A review of in situ observations of deformation-induced β ↔ α″ martensite transformations in metastable β Ti alloys, Adv. Eng. Mater. 24 (2022) 2200281, https://doi.org/10.1002/adem.202200281.

[50] Z. Liao, B. Luan, X. Zhang, R. Liu, K.L. Murty, Q. Liu, A multi-deformation mechanisms assisted metastable β-ZrTiAlV alloy exhibits high yield strength and high work hardening rate, J. Alloy. Compd. 816 (2020) 152642, https://doi.org/10.1016/j.jallcom.2019.152642.

[51] C. Wu, Q. Zhao, S. Huang, Y. Zhao, L. Lei, J. Ren, Q. Sun, L. Zhou, Deformation mechanisms in a β-quenched Ti-5321 alloy: in-situ investigation related to slip activity, orientation evolution and stress induced martensite, J. Mater. Sci. Technol. 112 (2022) 36–48, https://doi.org/10.1016/j.jmst.2021.09.051.

[52] X. Ma, Z. Chen, L. Xiao, S. Luo, W. Lu, Stress-induced martensitic transformation in a β-solution treated Ti–10V–2Fe–3Al alloy during compressive deformation, Mater. Sci. Eng.: A 801 (2021) 140404, https://doi.org/10.1016/j.msea.2020.140404.

[53] X.D. Wang, S.L. Song, D.M. Liu, Z.W. Zhu, H.F. Zhang, X.C. Ren, High fatigue endurance limit of a metastable Ti-based metallic glass composite with martensitic transformation, Intermetallics 136 (2021) 107253, https://doi.org/10.1016/j.intermet.2021.107253.

[54] J.F. Xiao, X.K. Shang, J.H. Hou, Y. Li, B.B. He, Role of stress-induced martensite on damage behavior in a metastable titanium alloy, Int. J. Plast. 146 (2021) 103103, https://doi.org/10.1016/j.ijplas.2021.103103.

[55] J. Long, X. Wei, Y. Dong, X. Cheng, H. Li, X. Xu, M. Zhu, In situ XPS analysis of tribo-chemical behavior in titanium alloy exposed to fretting wear under the vacuum environments, Tribology Lett. 72 (2024) 43, https://doi.org/10.1007/s11249-024-01842-8.

[56] S.K. Jha, K.S. Ravichandran, High-cycle fatigue resistance in beta-titanium alloys, JOM 52 (2000) 30–35, https://doi.org/10.1007/s11837-000-0097-x.

[57] R. Dong, H. Kou, Y. Zhao, X. Zhang, L. Yang, H. Hou, Morphology characteristics of α precipitates related to the crystal defects and the strain accommodation of variant selection in a metastable β titanium alloy, J. Mater. Sci. Technol. 95 (2021) 1–9, https://doi.org/10.1016/j.jmst.2021.01.090.

[58] N.A. Nochovnaya, A.A. Shiryaev, A.N. Andrianov, E.A. Davydova, Variability of hardening phase morphology and topology in pseudo-β-titanium alloys quenched for β-structure, Metallurgist 65 (2021) 633–642, https://doi.org/10.1007/s11015-021-01200-2.

[59] X. Ma, Z. Chen, L. Xiao, W. Lu, S. Luo, Y. Mi, Compressive deformation of a metastable β titanium alloy undergoing a stress-induced martensitic transformation: the role of β grain size, Mater. Sci. Eng.: A 794 (2020) 139919, https://doi.org/10.1016/j.msea.2020.139919.

[60] Z. Chen, D. Zhong, Q. Sun, X. Ma, Effect of α phase fraction on the dynamic mechanical behavior of a dual-phase metastable β titanium alloy Ti–10V–2Fe–3Al, Mater. Sci. Eng.: A 816 (2021) 141322, https://doi.org/10.1016/j.msea.2021.141322.

[61] R.D. Mindlin, Compliance of elastic bodies in contact, 529-268, J. Appl. Mech. 16 (1949), https://doi.org/10.1115/1.4009973.

[62] N.J. Kim, G. Thomas, Effects of morphology on the mechanical behavior of a dual phase Fe/2Si/0.1C steel, Metal. Mater. Trans. A 12 (1981) 483–489, https://doi.org/10.1007/BF02648546.
[63] X. Xu, W. Xu, F. Ederveen, S. v.d. Zwaag, Design of low hardness abrasion resistant steels, Wear 301 (2013) 89–93, https://doi.org/10.1016/j.wear.2013.01.002.
[64] O. Vingsbo, S. Söderberg, On fretting maps, Wear 126 (1988) 131–147, https://doi.org/10.1016/0043-1648(88)90134-2.
[65] N. Chen, H. Kou, Z. Wu, F. Qiang, K. Hua, C. Wang, B. Tang, J. Li, J.M. Molina-Aldareguia, Design of metastable β-Ti alloys with enhanced mechanical properties by coupling αs precipitation strengthening and TRIP effect, Mater. Sci. Eng.: A 835 (2022) 142696, https://doi.org/10.1016/j.msea.2022.142696.
[66] S.W. Lee, C.H. Park, J.-K. Hong, J.-T. Yeom, Development of sub-grained α+β Ti alloy with high yield strength showing twinning- and transformation-induced plasticity, J. Alloy. Compd. 813 (2020) 152102, https://doi.org/10.1016/j.jallcom.2019.152102.
[67] T. Grosdidier, Y. Combres, E. Gautier, M.J. Philippe, Effect of microstructure variations on the formation of deformation-induced martensite and associated tensile properties in a β metastable Ti alloy, Metall. Mater. Trans. A 31 (2000) 1095–1106, https://doi.org/10.1007/s11661-000-0105-3.
[68] Q.Y. Sun, S.J. Song, R.H. Zhu, H.C. Gu, Toughening of titanium alloys by twinning and martensite transformation, J. Mater. Sci. 37 (2002) 2543–2547, https://doi.org/10.1023/A:1015456026919.
[69] A. Paradkar, V. Kumar, S.V. Kamat, A.K. Gogia, B.P. Kashyap, The effect of grain size and composition on the fracture toughness of Ti–Al–Nb alloys undergoing stress-induced martensitic transformation, Mater. Sci. Eng.: A 486 (2008) 273–282, https://doi.org/10.1016/j.msea.2007.10.005.
[70] M. Mazinani, W.J. Poole, Effect of martensite plasticity on the deformation behavior of a low-carbon dual-phase steel, Metall. Mater. Trans. A 38 (2007) 328–339, https://doi.org/10.1007/s11661-006-9023-3.
[71] S. Kim, S. Lee, Effects of martensite morphology and volume fraction on quasi-static and dynamic deformation behavior of dual-phase steels, Metall. Mater. Trans. A 31 (2000) 1753–1760, https://doi.org/10.1007/s11661-998-0328-2.
[72] M. Sarwar, R. Priestner, Influence of ferrite-martensite microstructural morphology on tensile properties of dual-phase steel, J. Mater. Sci. 31 (1996) 2091–2095, https://doi.org/10.1007/BF00356631.
[73] H.Y. Kim, Y. Ikehara, J.I. Kim, H. Hosoda, S. Miyazaki, Martensitic transformation, shape memory effect and superelasticity of Ti-Nb binary alloys, Acta Mater. 54 (2006) 2419–2429, https://doi.org/10.1016/j.actamat.2006.01.019.
[74] X. Ma, F. Li, Z. Sun, J. Hou, X. Fang, Y. Zhu, C.C. Koch, Achieving gradient martensite structure and enhanced mechanical properties in a metastable β titanium alloy, Metall. Mater. Trans. A 50 (2019) 2126–2138, https://doi.org/10.1007/s11661-019-05157-5.
[75] X.X. Li, Y. Zhou, Y.X. Li, X.L. Ji, S.Q. Wang, Dry sliding wear characteristics of Ti-6.5Al-3.5Mo-1.5Zr-0.3Si alloy at various sliding speeds, Metall. Mater. Trans. A 46 (2015) 4360–4368, https://doi.org/10.1007/s11661-015-3019-9.